Hindawi
Mathematical Problems in Engineering
Volume 2020, Article ID 2106373, 9 pages
https://doi.org/10.1155/2020/2106373

Research Article

Mathematical Model of Cam Profile Based on Heald Frame Motion Characteristics

Honghuan Yin,[1] **Hongbin Yu**,[1] **Junqiang Peng**,[1] **and Hongyu Shao**[2]

[1]*School of Mechanical Engineering, Tianjin Polytechnic University, No. 399, Binshuixi Road, Xiqing District, Tianjin 300387, China*
[2]*School of Mechanical Engineering, Tianjin University, No. 92, Weijin Road, Nankai District, Tianjin 300072, China*

Correspondence should be addressed to Hongbin Yu; yuhongbin@tjpu.edu.cn

Received 12 October 2019; Revised 7 January 2020; Accepted 28 January 2020; Published 19 February 2020

Academic Editor: Andras Szekrenyes

Copyright © 2020 Honghuan Yin et al. This is an open access article distributed under the Creative Commons Attribution License, which permits unrestricted use, distribution, and reproduction in any medium, provided the original work is properly cited.

In this paper, the transmission process of the heald frame driven by the dobby is analyzed. The equivalent motion model of the dobby modulator, the eccentric mechanism, and the motion transmission unit are constructed. Then, based on the given movement characteristics of the heald frame, the mathematical model is built to achieve the cam pitch curve and the cam profile of the modulator. The numerical solution method for this is developed. The preparation of a mathematical model for the new concept of the solving cam profile based on the motion characteristics of heald frames is explained in this study. By setting a 11th polynomial motion law of the heald frame, due to the inconsistency between the outward and return motion laws of the crank-rocker mechanism, an asymmetrical cam profile is obtained under the premise of ensuring that the heald frame's ascending and descending motions are consistent. Through the kinematics simulation analysis, the correctness of the reverse process is verified.

1. Introduction

At present, the weaving technology is focused towards higher speeds, higher efficiency, and easier control and operation [1, 2]. Eren [3–6] introduced kinematic models for the motion of rotary dobbies, cranks, and cam shedding mechanisms, and equations governing heald frame motion were derived. In addition, the obtained heald frame motion curves were compared with each other, while the heald frame motion characteristics were mainly determined the design of the modulator mechanism. Nowadays, in modern high-speed weaving machines, rotary dobbies have been developed for the shedding operations. Rotary dobbies convert the rotational motion of the main shaft of the weaving machine into an up-down frame motion by means of various gears, arms, and eccentrics (cams) [7, 8].

In optimal cam profile design, particularly focused on reducing vibration, Wiederrich [9–11] has been the subject of numerous investigations. Stoddart [12–15] continued Dudley's work on polydyne cams for valve trains and developed a characteristic relationship between vibration amplitude and cam speed. Mermelstein and Acar [16] used piecewise polynomials, and the complete cam profile can be designed as a combined linear system. Qiu, et al. [17] generated optimized motion curves using B-splines and simultaneously handled many design objectives, including the control of residual vibrations. Mosier [18–21] started with a candidate acceleration function that was adjusted to satisfy the necessary constraints. In that method, no candidate profile was needed and all of the desired acceleration properties were defined from the outset with no adjustments needed to produce the final form. The result was better control over all important acceleration events during the cam cycle. Once the acceleration was defined, the velocity was obtained by integrating the acceleration while enforcing boundary conditions and continuity between segments [22].

However, no other publications found the research of relationship between heald frame movement and cam profile in the literature. In particular, the cam profile is calculated based on the motion characteristics of the heald frame. This paper conducts a research study on the construction of the

cam profile of the modulator through mathematical models based on the heald frame motion characteristics.

2. Motion Principle

The rotary dobby and heald frame shedding control mechanism consist of a modulator, an eccentric mechanism, a motion transmission unit (MTU), and a heald frame. The motion principle is presented in Figure 1. The modulator is used to convert the continuous rotation of the loom main shaft into an intermittent movement of the shaft. The schematic view of the modulator is shown in Figure 1(a). The conjugate cam (5 and 10) is fixed to the dobby body. The cam follower arms (2 and 8) that are used as an engagement element are pivoted on gear 1 and can rotate around its pivot axis O_1, transmitting the motion of the loom to the cam rollers (3, 6, 9, and 12). The rotation of the follower rollers makes links 4 and 7 to move and drive the main shaft 11. Therefore, the modulator transforms the uniform rotary motion of the weaving machine into a nonuniform rotary motion of the main shaft.

Figure 1(b) illustrates the schematic views of the eccentric mechanism, MTU, and heald frame. The link 13 is an eccentric disc cam, as its center of rotation O_1 is different from its geometrical center D. Due to this characteristic, when the gear of the modulator rotates, for example, clockwise, the motion of the main shaft is transmitted to the eccentric disc cam and its motion is transmitted to the lifting arm 15 by the ring link 14. The motion of link 15 is transmitted to the heald frame by the MTU (Figure 1(b)). The MTU consists of a four-bar linkage mechanism (O_2FGO_3, MTU-I) and a crank slider mechanism (O_3HI, MTU-II). The forwardmost and rearmost positions of the lifting arm 15 correspond to the lower and higher positions of the heald frame 21, respectively. Due to this construction, the eccentric mechanism generates a heald frame motion only for plain weaving. In order to convert it to a rotary dobby mechanism, it is necessary to include the necessary means to get the lifting arm 15 (hence, the heald frame) dwelt at its forwardmost and rearmost positions as many loom revolutions as required by the weave [3].

3. Mathematical Model of the Shedding Motion

3.1. MTU and Heald Frame Modeling. The schematic diagram of MTU is shown in Figure 2. MTU-II is equivalent to a slider-crank linkage that changes at each position, and the kinematic characteristics of the heald frame are transformed to those of the crank 14 and the link 13. The link 11 is rigidly coupled to the link 13. The angle between them is φ_9 around the fixed point O_3. The positive angle between the link 13 and the x axis is φ_{10}.

Stoddart [12] demonstrated how to develop double-dwell polynomials suitable for polydyne applications. Define $L(u) = S(u) + S_0$ as the kinematic characteristic function of the heald frame (15), where e is the offset of the slider 15, S_0 is the distance between the initial point I and the x axis. $l_{13} = O_3H$, and $l_{14} = HI$. e, S_0, l_{13}, and l_{14} are known parameters in the slider-crank mechanism (O_3HI). $S(u)$ is an 11th-degree polynomial [23] motion law and is described as follows:

$$S(u) = h\left(336u^5 - 1890u^6 - 4740u^7 - 6615u^8 + 5320u^9 - 2310u^{10} + 420u^{11}\right). \tag{1}$$

The straight-line motion of the heald frame is transformed from the rotational motion of the link 13. The displacement equation, relating the parameters e, l_{14}, and l_{13} to the input and output variables $L(u)$ and φ_{10}, may be written as [24]

$$2l_{13}\left[L(u)\sin\varphi_{10} - e\cos\varphi_{10}\right] + l_{14}^2 - \left[l_{13}^2 + L^2(u) + e^2\right] = 0, \tag{2}$$

$$\varphi_{10} = \arcsin\left[\frac{\left(l_{13}^2 + L^2(u) + e^2 - l_{14}^2\right)}{2l_{13}\sqrt{L^2(u) + e^2}}\right] + \arctan\left(\frac{e}{L(u)}\right), \quad \text{for } \varphi_{10} \in \left(-90^\circ, 90^\circ\right). \tag{3}$$

Equation (3) takes a derivative of time and obtains angular velocity of φ_{10}:

$$\omega_{10} = -\frac{2L(u)\cdot\left[\mathrm{d}L(u)/\mathrm{d}u\right] + 2l_{15}L(u)\sin\varphi_{10}}{2l_{13}\left[L(u)\cos\varphi_{10} + e\sin\varphi_{10}\right]}. \tag{4}$$

MTU-I is also equivalent to a four-bar linkage mechanism that changes its geometry at each position (Figure 2). Angle φ_{10} of the link 13 can be obtained from equations (1) to (4). Angle φ_8 of the link 11 can be obtained by the geometric relationship $\varphi_8 = \varphi_9 + \varphi_{10}$, where φ_5 and φ_9 are the known parameters.

In this study, l_{12} represents the distance from the point O_3 to the pivot point O_2, l_{11} represents the input link length of O_3G, l_{10} represents the link length of FG, and l_9 represents the output link length of O_2F. If a Cartesian coordinate system (X, Y) is centered on the pivot point O_3, then angle φ_6 can be expressed in terms of φ_8.

The complex vector form of the closed vector equation is defined as

$$l_9e^{i\varphi_6} + l_{10}e^{i\varphi_7} = l_{11}e^{i\varphi_8} + l_{12}. \tag{5}$$

The Euler formula is applied:

$$e^{i\varphi} = \cos\varphi + i\sin\varphi. \tag{6}$$

The real part is separated from the imaginary part of equation (5), yielding

$$\begin{cases} l_9\cos\varphi_6 + l_{10}\cos\varphi_7 = l_{11}\cos\varphi_8 + l_{12}, \\ l_9\sin\varphi_6 + l_{10}\sin\varphi_7 = l_{11}\sin\varphi_8. \end{cases} \tag{7}$$

Angle φ_7 is eliminated to get

$$l_{10}^2 = l_{11}^2 + l_{12}^2 + l_9^2 + 2l_{11}l_{12}\cos\varphi_8 - 2l_9l_{12}\cos\varphi_6 - 2l_9l_{11}\cos(\varphi_8 - \varphi_6), \tag{8}$$

$$2\left[l_{12}\left(l_{11}\cos\varphi_8 - l_9\cos\varphi_6\right) - l_{11}l_9\left(\varphi_8 - \varphi_6\right)\right] + l_{12}^2 + l_{11}^2 - l_{10}^2 + l_9^2 = 0. \tag{9}$$

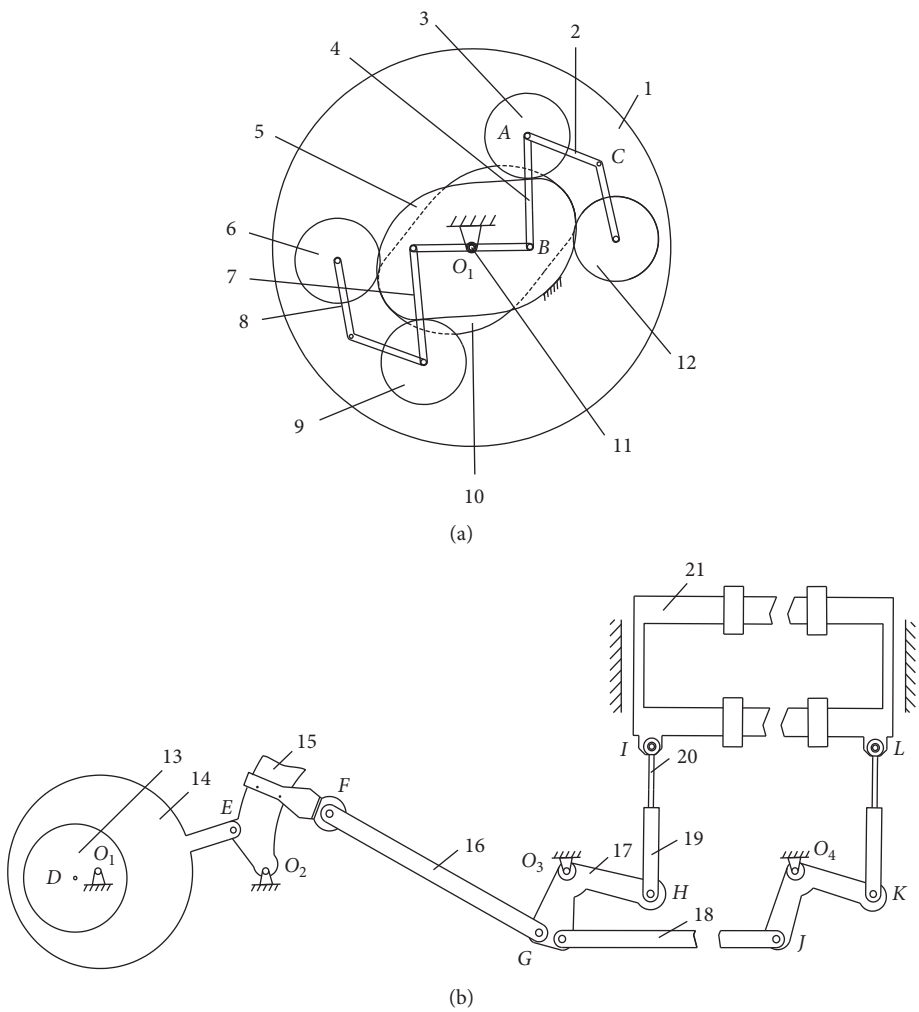

Figure 1: Heald frame motion principle. (a) Modulator. (1) gear; (2, 8), cam swing arms; (3, 6, 9, 12) cam rollers; (4, 7) modulator links; (5, 10) conjugate cams; and (11) main shaft. (b) Eccentric mechanism, MTU, and heald frame. (13) Eccentric disc cam; (14) ring link; (15) lifting arm; (16) lifting arm link; (17) swivel arm; (18) rotor link; (19) heald frame link; (20) support link; and (21) heald frame.

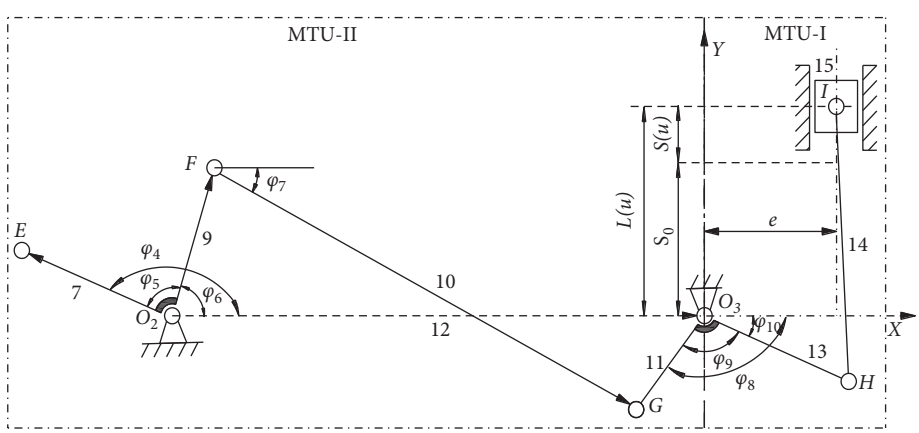

Figure 2: Schematic diagram of the MTU.

After some manipulation and substitution, the final result is

$$\tan\left(\frac{\varphi_6}{2}\right) = \frac{\left(B - \sqrt{A^2 + B^2 - C^2}\right)}{(A - C)}, \tag{10}$$

where $A = l_{12} + l_{11}\cos\varphi_8$, $B = l_{11}\sin\varphi_8$, and $C = (A^2 + B^2 + l_9^2 - l_{10}^2)/2l_9$.

$$\varphi_6 = 2\arctan\left[\frac{\left(B - \sqrt{A^2 + B^2 - C^2}\right)}{(A - C)}\right], \quad \text{for } \varphi_6 \in \left(0^\circ, 90^\circ\right). \tag{11}$$

Equation (7) is differentiated by time and gives

$$\begin{cases} l_9\omega_6\sin\varphi_6 + l_{10}\omega_7\sin\varphi_7 = l_{11}\omega_8\sin\varphi_8, \\ l_9\omega_6\cos\varphi_6 + l_{10}\omega_7\cos\varphi_7 = l_{11}\omega_8\cos\varphi_8. \end{cases} \tag{12}$$

Equation (12) is written as a matrix:

$$\begin{bmatrix} l_9\sin\varphi_6 & l_{10}\sin\varphi_7 \\ l_9\cos\varphi_6 & l_{10}\cos\varphi_7 \end{bmatrix}\begin{bmatrix} \omega_6 \\ \omega_7 \end{bmatrix} = \omega_8\begin{bmatrix} l_{11}\sin\varphi_8 \\ l_{11}\cos\varphi_8 \end{bmatrix}. \tag{13}$$

From equation (13), the ω_6 and ω_7 angular velocity functions can be derived:

$$\omega_6 = \frac{\omega_8 l_{11}\sin(\varphi_7 - \varphi_8)}{l_9\sin(\varphi_7 - \varphi_6)}, \tag{14}$$

$$\omega_7 = \frac{\omega_8 l_{11}\sin(\varphi_8 - \varphi_6)}{l_{10}\sin(\varphi_6 - \varphi_7)}. \tag{15}$$

Equation (13) is differentiated by time and gives

$$\begin{aligned} &\begin{bmatrix} l_9\sin\varphi_6 & l_{10}\sin\varphi_7 \\ l_9\cos\varphi_6 & l_{10}\cos\varphi_7 \end{bmatrix}\begin{bmatrix} \alpha_6 \\ \alpha_7 \end{bmatrix} \\ &\quad = -\begin{bmatrix} l_9\cos\varphi_6 & l_{10}\cos\varphi_7 \\ -l_9\sin\varphi_6 & -l_{10}\sin\varphi_7 \end{bmatrix}\begin{bmatrix} \omega_6 \\ \omega_7 \end{bmatrix} \\ &\qquad + \alpha_8\begin{bmatrix} l_{11}\sin\varphi_8 \\ l_{11}\cos\varphi_8 \end{bmatrix} + \omega_8\begin{bmatrix} l_{11}\cos\varphi_8 \\ -l_{11}\sin\varphi_8 \end{bmatrix}. \end{aligned} \tag{16}$$

The α_6 and α_7 theoretical anger acceleration functions of the follower, respectively, are

$$\alpha_6 = \frac{\omega_6^2 l_9\cos(\varphi_6 - \varphi_7) + \omega_7^2 l_{10} - \omega_8^2 l_{11}\cos(\varphi_8 - \varphi_7)}{l_{11}\sin(\varphi_8 - \varphi_7)}, \tag{17}$$

$$\alpha_7 = \frac{-\omega_6^2 l_9\cos(\varphi_6 - \varphi_8) - \omega_7^2 l_{10}\cos(\varphi_7 - \varphi_8) - \omega_8^2 l_{11}}{l_{11}\sin(\varphi_7 - \varphi_8)}. \tag{18}$$

3.2. Eccentric Mechanism Modeling. Figure 3 illustrates the eccentric mechanism, which is equivalent to a crank-rocker mechanism. From equations (5) to (18), the φ_6 angular motion characteristic functions can be obtained. φ_4 is considered to affect the output of the φ_2. According to Figure 3, $\varphi_4 = \varphi_6 + \varphi_5$, where φ_5 is a known parameter.

Moreover, l_8 represents the distance from the pivot point O_2 to the pivot point O_1, l_7 represents the lifting arm length of O_2E, l_6 represents the link length of ED, and l_5 represents the output link length of O_1D. During one revolution of the link 5, the lifting arm 7 swings between its limit positions and the swing angle is $\varnothing$. When points O_1, D_0, and E are on the same line and O_1D_0 and D_0E are extended, the lifting arm 7 reaches its forwardmost position. When O_1D_0 and D_0E are folded on top of each other, the link 7 reaches its rearmost position. The eccentric mechanism has no quick-return characteristics.

If a Cartesian coordinate system (X, Y) is centered on the pivot point O_2, the output angle φ_2 can be expressed in terms of φ_4:

$$\begin{cases} l_5\cos\varphi_2 + l_6\cos\varphi_3 = l_7\cos\varphi_4 + l_8, \\ l_5\sin\varphi_2 + l_6\sin\varphi_3 = l_7\sin\varphi_4. \end{cases} \tag{19}$$

Then,

$$\begin{aligned} l_6^2 = {} & l_7^2 + l_8^2 + l_5^2 + 2l_7l_8\cos\varphi_4 - 2l_5l_8\cos\varphi_2 \\ & - 2l_5l_7\cos(\varphi_4 - \varphi_2). \end{aligned} \tag{20}$$

Then,

$$\begin{aligned} & 2\left[l_8\left(l_7\cos\varphi_4 - l_5\cos\varphi_2\right) - l_7l_5\cos(\varphi_4 - \varphi_2)\right] \\ & \quad + l_8^2 + l_7^2 - l_6^2 + l_5^2 = 0. \end{aligned} \tag{21}$$

After some manipulation and substitution, the final result is

$$\tan\left(\frac{\varphi_2}{2}\right) = \frac{\left(B \pm \sqrt{A^2 + B^2 - C^2}\right)}{(A - C)}, \tag{22}$$

where $A = l_8 + l_7\cos\varphi_4$, $B = l_7\sin\varphi_4$, and $C = A^2 + B^2 + l_5^2 - l_6^2/2l_5$.

$$\varphi_2 = 2\arctan\left[\frac{\left(B \pm \sqrt{A^2 + B^2 - C^2}\right)}{(A - C)}\right], \quad \text{for } \varphi_2 \in \left[-180^\circ, 180^\circ\right). \tag{23}$$

Equation (19) is differentiated by time and gives

$$\begin{cases} l_5\omega_2\sin\varphi_2 + l_6\omega_3\sin\varphi_3 = l_7\omega_4\sin\varphi_4, \\ l_5\omega_2\cos\varphi_2 + l_6\omega_3\cos\varphi_3 = l_7\omega_4\cos\varphi_4. \end{cases} \tag{24}$$

Equation (24) is written as a matrix:

$$\begin{bmatrix} l_5\sin\varphi_2 & l_6\sin\varphi_3 \\ l_5\cos\varphi_2 & l_6\cos\varphi_3 \end{bmatrix}\begin{bmatrix} \omega_2 \\ \omega_3 \end{bmatrix} = \omega_4\begin{bmatrix} l_7\sin\varphi_4 \\ l_7\cos\varphi_4 \end{bmatrix}. \tag{25}$$

From equation (25), the ω_2 and ω_3 angular velocity functions can be derived:

$$\omega_2 = \frac{\omega_4 l_7\sin(\varphi_3 - \varphi_4)}{l_5\sin(\varphi_3 - \varphi_2)}, \tag{26}$$

$$\omega_3 = -\frac{\omega_4 l_7\sin(\varphi_4 - \varphi_2)}{l_6\sin(\varphi_2 - \varphi_3)}. \tag{27}$$

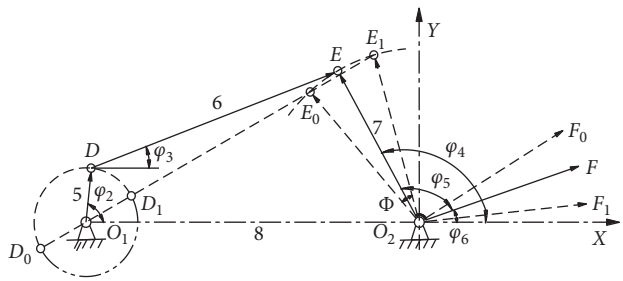

Figure 3: Schematic diagram of the eccentric mechanism.

Equation (25) is differentiated by time and gives

$$\begin{bmatrix} l_5 \sin\varphi_2 & l_6 \sin\varphi_3 \\ l_5 \cos\varphi_2 & l_6 \cos\varphi_3 \end{bmatrix} \begin{bmatrix} \alpha_2 \\ \alpha_3 \end{bmatrix} = \alpha_4 \begin{bmatrix} l_7 \sin\varphi_4 \\ l_7 \cos\varphi_4 \end{bmatrix} + \omega_4 \begin{bmatrix} l_7 \cos\varphi_4 \\ -l_7 \sin\varphi_4 \end{bmatrix} - \begin{bmatrix} l_5 \cos\varphi_2 & l_6 \cos\varphi_3 \\ -l_5 \sin\varphi_2 & -l_6 \sin\varphi_3 \end{bmatrix} \begin{bmatrix} \omega_2 \\ \omega_3 \end{bmatrix}. \tag{28}$$

The α_2 and α_3 angular acceleration functions are

$$\alpha_2 = \frac{\omega_2^2 l_5 \cos(\varphi_2 - \varphi_3) + \omega_3^2 l_6 - \omega_4^2 l_7 \cos(\varphi_4 - \varphi_3)}{l_7 \sin(\varphi_4 - \varphi_3)}, \tag{29}$$

$$\alpha_3 = \frac{-\omega_2^2 l_5 \cos(\varphi_2 - \varphi_4) - \omega_3^2 l_6 \cos(\varphi_3 - \varphi_4) - \omega_4^2 l_7}{l_7 \sin(\varphi_3 - \varphi_4)}. \tag{30}$$

3.3. Modulator Modeling. Figure 4 shows a schematic diagram of the cam-link modulator. Angle φ_2 of the link O_1D can be obtained from equations (19) to (30). Angle φ_2 is equal to angle φ_1, $\varphi_1 = \varphi_2$, where φ_1 is the main shaft angle of the modulator.

In Figure 4(a), ω is the angular velocity of the gear. The starting position of the cam swing arm coincides with the hinge point C of the gear. A Cartesian coordinate system (X, Y) is centered on the cam point O_1. The rotation angle of the gear in the Cartesian coordinate system is defined as θ, and it is expressed by $\theta = \omega t$ (Figure 4(b)).

From the geometric relationship,

$$\begin{cases} (x_A - x_B)^2 + (y_A - y_B)^2 = l_2^2, \\ (x_A - x_C)^2 + (y_A - y_C)^2 = l_1^2. \end{cases} \tag{31}$$

Then,

$$\begin{cases} x_A = \dfrac{\left(-B_1 \pm \sqrt{B_1^2 - 4A_1C_1}\right)}{2A_1}, \\ y_A = \dfrac{(C - Ax)}{B}, \end{cases} \tag{32}$$

where $A = x_C - x_B$, $B = y_C - y_B$, $C = (l_4 - l_3 - x_B^2 - y_B^2 + x_C^2 + y_C^2)/2$, $A_1 = A^2 + B^2$, $B_1 = 2ABy_B - 2AC - 2B^2x_B$, $C_1 = -2BCy_B + C^2 - B^2(l_4^2 - y_B^2 - x_B^2)$, $x_B = l_3 \cos\varphi_1$, $y_B = l_3 \sin\varphi_1$, $x_c = l_4 \cos\theta$, and $y_c = l_4 \sin\theta$.

The distance between the cam actual profile and the cam pitch curve is equal to the roller radius r. The cam profile along a direction normal to any point A is taken as a distance r in order to obtain the coordinates of the corresponding point $T(x_T, y_T)$ on the actual cam profile.

The slope of the normal line $n - n$ at the cam pitch curve A is

$$\tan\gamma = \frac{dx_A}{dy_A} = -\frac{(dx_A/d\theta)}{(dy_A/d\theta)} = \frac{\sin\gamma}{\cos\gamma}, \tag{33}$$

where γ is the angle between the normal line $n - n$ and the x axis and (x_A, y_A) are the coordinates of any point A on the cam pitch curve.

Equation (33) can be written as

$$\begin{cases} \sin\gamma = \dfrac{(dx_A/d\theta)}{\sqrt{(dx_A/d\theta)^2 + (dy_A/d\theta)^2}}, \\ \cos\gamma = -\left(\dfrac{(dy_A/d\theta)}{\sqrt{(dx_A/d\theta)^2 + (dy_A/d\theta)^2}}\right). \end{cases} \tag{34}$$

According to equations (31) to (34), the coordinates of the point $T(x_T, y_T)$ of the actual cam profile can be worked out as follows:

$$\begin{cases} x_T = x_A \pm r\cos\gamma, \\ y_T = y_A \pm r\cos\gamma. \end{cases} \tag{35}$$

From equations (31) to (35), the analytical solution of the cam profile equation can be determined computationally.

4. Results and Discussion

4.1. Calculation. A mathematical model was used to ascertain the relationship between heald frame motion characteristics and cam profile. In the calculation process, the program was written in Visual Studio 2012 and ran on a personal computer.

Figure 5 shows the kinematic curves of the heald frame for displacement, velocity, acceleration, and jerk [20] for the 11th-degree polynomial functions. These polynomial functions are taken as the motion characteristics (Displac-11th, Velocity-11th, Accel-11th, and Jerk-11th) of the heald frame in combination with equation (1). The program sets 180°/2000 as the rotation step of the gear and calculates from 0° to 180°.

According to the actual size of the test bench as shown in Figure 6, the parameter h is 106.8 mm; the length of l_{14} is 375 mm, e is 200 mm, the fixed angle φ_9 is 97.65°, the length of l_{13} is 200 mm, and the distance S_0 is 325 mm.

This program employed equations (1) to (4) and used the above parameter values as input data, and the φ_{10} motion characteristics (Angular displac-φ_{10}, Angular velocity-φ_{10}, Angular accel-φ_{10}, and Jerk-φ_{10}) can be obtained and are presented in Figure 7, normalized with respect to the calculated maximum angular displacement value of 31°. Results are shown for the half gear cycle only, after which a steady state is achieved.

Based on the test bench, the length of link l_{11} is 150 mm, the length of l_{12} is 695 mm, the length of l_{10} is 550 mm, the

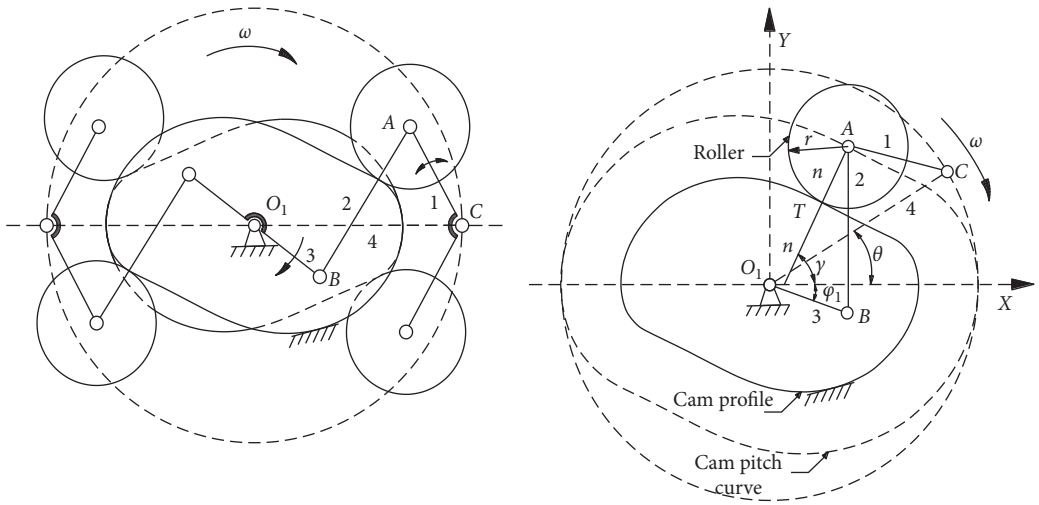

(a) (b)

Figure 4: Cam-link modulator.

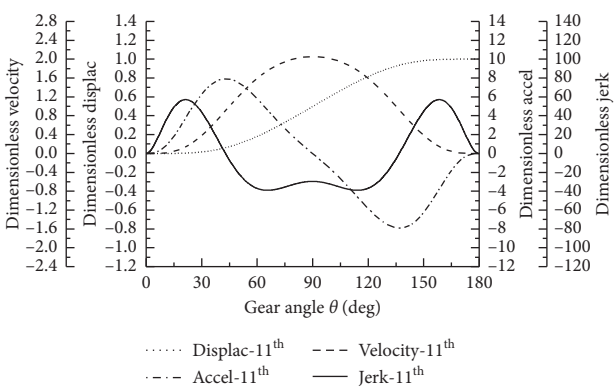

Figure 5: 11th-degree polynomial curves.

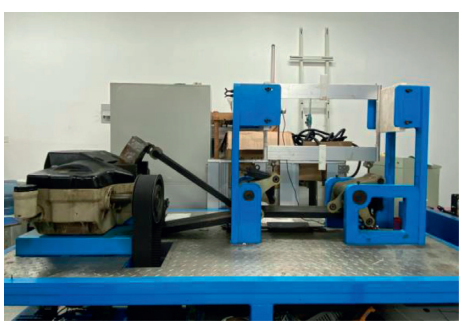

Figure 6: The test bench.

fixed angle φ_5 is 100°, and the length of link l_9 is 185 mm. According to equations (5) to (18) and the above parameter values, the φ_6 motion characteristics (Angular displac-φ_6, Angular velocity-φ_6, Angular accel-φ_6, and Jerk-φ_6) can be obtained and the results are presented in Figure 8, normalized with respect to the maximum angular displacement value of 36.4°.

The length of link l_5 is 30 mm, the length of l_6 is 170 mm, and the length of link l_7 is 96 mm. In order to ensure no quick-return motion of eccentric mechanism, the length of

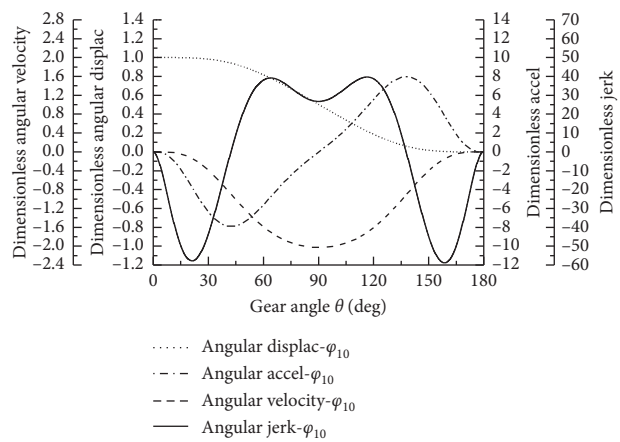

Figure 7: Motion characteristics of angular φ_{10}.

l_8 is calculated to be 192.94 mm. According to equations (19) to (30) and the above parameter values, when D_0 moves counterclockwise and clockwise to D_1, the φ_2 motion characteristics (Angular displac-$\varphi_2 - 1$, Angular velocity-$\varphi_2 - 1$, Angular accel-$\varphi_2 - 1$, and Angular jerk-$\varphi_2 - 1$) and (Angular displac-$\varphi_2 - 2$, Angular velocity-$\varphi_2 - 2$, Angular accel-$\varphi_2 - 2$, and Angular jerk-$\varphi_2 - 2$) are obtained, respectively, which are presented in Figure 9, normalized with respect to the maximum angular displacement value of 180°.

The length of l_3 is 42.5 mm, the length of l_4 is 111 mm, the length of l_2 is 81 mm, and the length of l_1 is 56 mm. In Figure 4, the rotation angle θ of the gear is ωt, and the step is 180°/2000, $\theta \in [0°, 180°)$. According to equations (31) to (35) and the above parameter values, the 2000 points are obtained through the program. The final cam profiles 1 and 2 and cam pitch curves 1 and 2 fitted through nonuniform rational B-splines (NURBS) can be established. They are presented in Figure 10.

4.2. Simulation. In order to verify the correctness of the proposed mathematical model, a virtual prototype of the rotary dobby and the heald frame shedding control

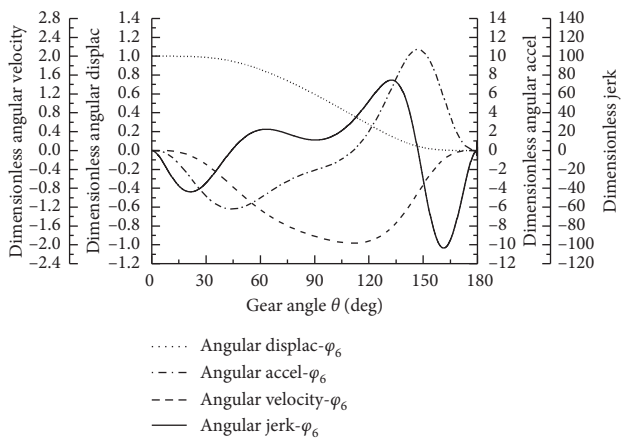

Figure 8: Motion characteristics of angular φ_6.

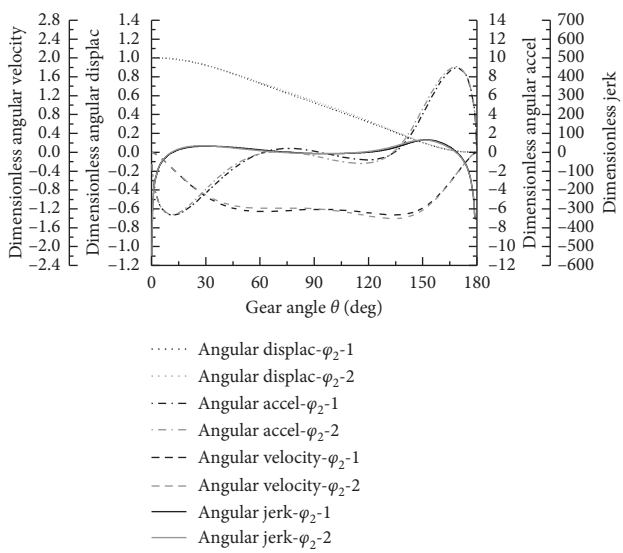

Figure 9: Motion characteristics of angular φ_2.

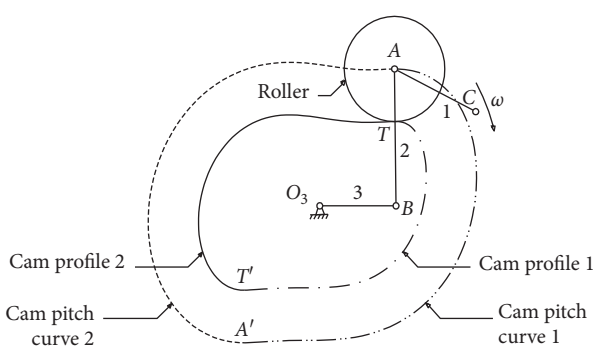

Figure 10: Cam profile and cam pitch curve 1 and 2.

mechanism is developed using SolidWorks 2016. The noncentral symmetrical cam defined by the cam profile curve 1 and 2 is employed on the modulator. The motion simulation is performed on the heald frame driven by the rotary dobby with this modulator. The obtained simulation characteristics (Displac-SHF, Velocity-SHF, Accel-SHF, and Jerk-SHF) of the heald frame are compared with the

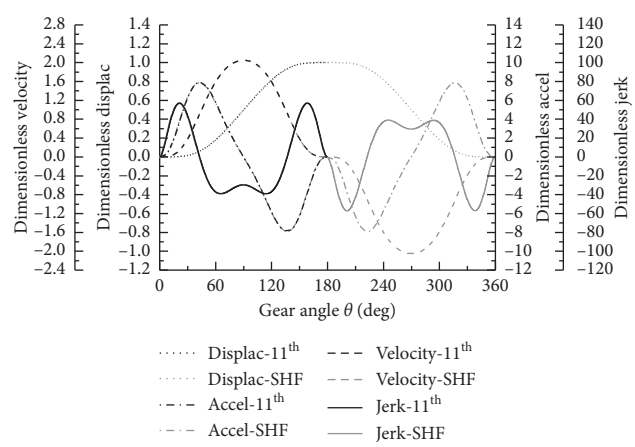

Figure 11: 11th-degree polynomial curves and simulation characteristics of the heald frame.

characteristics (Displac-11th, Velocity-11th, Accel-11th, and Jerk-11th) (Figure 11).

As it can be seen in Figure 12, the period of the gear is 180° and the modulator shedding motion characteristics (Displac-SHF, Velocity-SHF, Accel-SHF, and Jerk-SHF) of the heald frame are very close to the 11th polynomial curves, which proves the correctness of the proposed mathematical model. At the same time, the main shaft of the rotary dobby is rotated for one cycle and the same heald motion characteristics as motion characteristics (Displac-SHF, Velocity-SHF, Accel-SHF, and Jerk-SHF) can be formed, meaning that regardless the forward or reverse rotation of the gear, the heald frame rise laws are consistent with the fall laws.

The cam profile 3 and 4 are formed by copying and rotating the cam profile 1 and 2 by 180° and combining them (Figure 12), whereas the cam profile 3 is shown as the dash dot line and the cam profile 4 is shown as the solid line. The cam pitch curve 3 and 4 are shown as the dash double-dot line and the dashed line, respectively.

The two cams formed by cam profile 3 and 4 are employed in the modulator. The two cams are mounted on the rotary dobby transmission mechanism in order to obtain the movement law of the heald frame. Motion characteristics

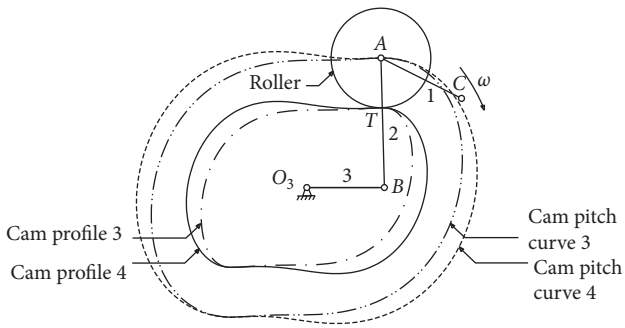

Figure 12: Cam profile and cam pitch curve 3 and 4.

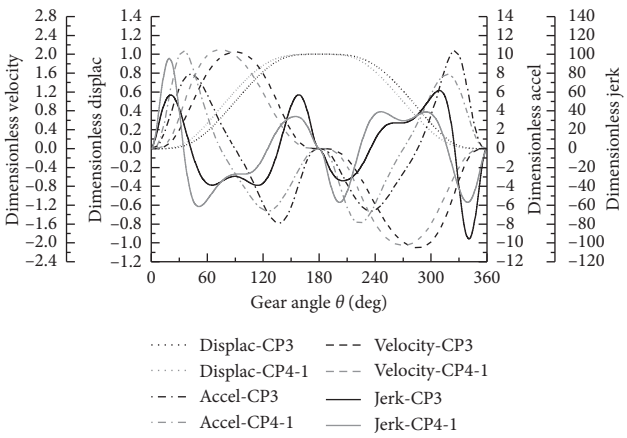

Figure 13: The motion characteristics of the heald frame with the same rotation direction.

(Displac-CP3, Velocity-CP3, Accel-CP3, and Jerk-CP3; Displac-CP4-1, Velocity-CP4-1, Accel-CP4-1, and Jerk-CP4-1) are obtained from the simulation of the heald frame motion driven by the rotary dobby with the aforementioned modulators, $\theta \in [0^{\circ}, 360^{\circ})$. The results are compared with each other and presented in Figure 13.

It can be seen that the motion characteristics (Displac-CP3, Velocity-CP3, Accel-CP3, and Jerk-CP3; Displac-CP4-1, Velocity-CP4-1, Accel-CP4-1, and Jerk-CP4-1) of the heald frame formed by cam profiles 3 and 4, respectively, are very different. Figure 14 shows the deviation curves. The motion of the heald frame by the modulator with cam profile 3 or 4 resulted in different characteristics in the upward and downward sections. More specifically, the forward and reverse rotation of the dobby modulator main shaft resulted in different heald frame motion characteristics.

However, in Figure 15, the heald frame motion characteristics (Displac-CP3, Velocity-CP3, Accel-CP3, and Jerk-CP3) generated by the dobby modulator when it rotates forward with cam profile 3 and the movement characteristics (Displac-CP4-2, Velocity-CP4-2, Accel-CP4-2, and Jerk-CP4-2) generated by the dobby modulator when it rotates reversely with cam profile 4 are compared. As it can be observed, the values of motion characteristics (Displac-CP3, Velocity-CP3, Accel-CP3, and Jerk-CP3; Displac-CP4-2, Velocity-CP4-2, Accel-CP4-2, and Jerk-CP4-2) have the same variation trend. This implies that modulators with

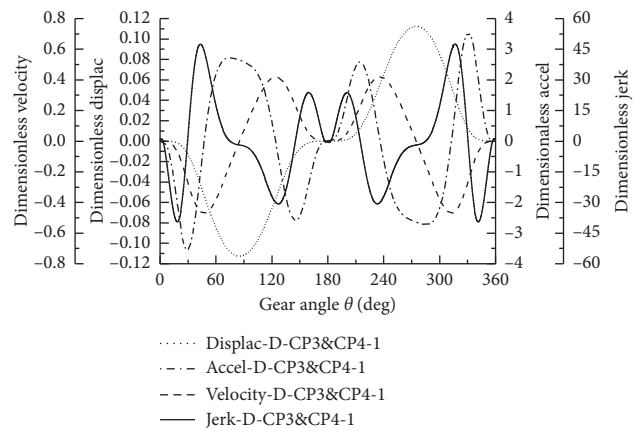

Figure 14: The deviations of motion characteristics.

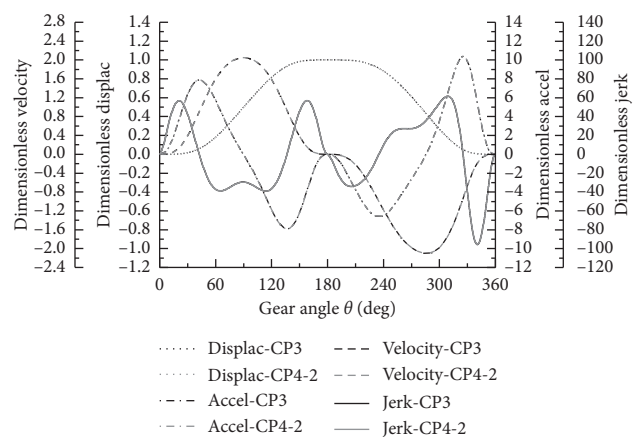

Figure 15: The motion characteristics of the heald frame with different rotation directions.

different cam profiles can produce exactly the same heald frame motion characteristics.

The above findings form the foundation for the modulator design and further theoretical analysis of the rotary dobby structure.

5. Conclusions

When the geometric dimensions of the modulator, eccentric mechanism, and MTU, as well as the motion curve, of the heald frame are given, the analytical mathematical model of the cam profile and the cam pitch curve can be determined. In this mathematical model, it is possible to ascertain the relationship between heald frame motion characteristics and cam profile. By means of this model, 2000 points of cam profile is obtained, and the error of this model can be reduced by increasing the number of calculation points. The model proposed in this article enables the analysis of the heald frame motion characteristics and the cam profile design. Given different heald frame displacement curves and parameter values, the cam profile and motion characteristics of each motion transfer process can be obtained based on the proposed mathematical model.

Based on the particularity of the rotary dobby structure, a cam profile is obtained, and the motion law of the heald frame is solved in the forward direction to verify the correctness of the inverse model. At the same time, regardless of whether the dobby is rotating forward or backward, the motion of the heald frame is the same, while the cam is asymmetrical.

Two cam profiles are obtained, the heald frame motion characteristics are solved in the forward direction, and the asymmetric motion characteristics of the heald frame are obtained. The asymmetric deviation revealed the cam profiles, the eccentric mechanism, and the motion transmission mechanism. When the roller moves clockwise along one of the cam profiles and counterclockwise along the other cam profile, the exact same heald frame motion characteristics are produced.

A good correlation is found between the simulation and calculation results of the heald frame displacement, velocity, acceleration, and jerk. Future work will include the development of a virtual prototype, which will verify the mathematical model and may give a wealth of dynamic information about the system, as well as similar systems yet to be built.

Data Availability

All data's used to support the findings of this study are included within the article.

Disclosure

Honghuan Yin and Hongbin Yu are co-first authors.

Conflicts of Interest

The authors declare that they have no conflicts of interest.

Acknowledgments

This research was supported by the National Key R&D Program of China (2017YFB1104202).

References

[1] Anon, "Rotary dobby-the efficient shed forming mechanism for modern weaving machines," *International Textile Bulletin, Fabric Forming*, vol. 66, pp. 45-46, 1983.

[2] R. Marks and A. T. C. Robinson, *Principles of Weaving*, The Textile Institute, London, UK, 1976.

[3] R. Eren, G. Ö enA, and Y. Turhan, "Kinematics of rotary dobby and analysis of heald frame motion in weaving process," *Textile Research Journal*, vol. 78, no. 12, pp. 1070–1079, 2008.

[4] Staubli Dobby machines catalog, 2006.

[5] P. A. Korolev and V. N. Lohmanov, "Kinematics of connections of the shedding mechanism of a circular loom TKP-110-U," *Lzvestiya Vysshikh Uchebnykh Zavedenii, Seriya Teknologiya*, vol. 4, pp. 116–119, 2011.

[6] K. Sadettin, D. M. Taylan, and K. Ali, "Cam motion tuning of shedding mechanism for vibration reduction of heald frame," *Gazi University Journal of Science*, vol. 23, no. 2, pp. 227–232, 2010.

[7] G. Abdulla and O. Can, "Design of a new rotary dobby mechanism," *Industria Textile*, vol. 69, no. 6, pp. 429–433, 2018.

[8] D. Mundo, G. A. Danieli, and H. S. Yan, "Kinematic optimization of mechanical presses by optimal synthesis of cam-integrated linkages," *Transactions of the Canadian Society for Mechanical Engineering*, vol. 30, no. 4, pp. 519–532, 2006.

[9] J. L. Wiederrich, *Design of cam profiles for systems with high inertial loading*, Ph.D. thesis, Stanford University, Stanford, CA, USA, 1973.

[10] M. Chew and C. H. Chuang, "Minimizing residual vibrations in high-speed cam-follower systems over a range of speeds," *Journal of Mechanical Design*, vol. 117, no. 1, pp. 166–172, 1995.

[11] K. C. Gupta and J. L. Wiederrich, "Development of cam profiles using the convolution operator," *Journal of Mechanisms, Transmissions, and Automation in Design*, vol. 105, no. 4, pp. 654–657, 1983.

[12] D. A. Stoddart, "Polydyne cam design-I," *Machine Design*, vol. 1, pp. 121–135, 1953.

[13] D. A. Stoddart, "Polydyne cam design-II," *Machine Design*, vol. 2, pp. 146–154, 1953.

[14] D. A. Stoddart, "Polydyne cam design-III," *Machine Design*, vol. 3, pp. 149–164, 1953.

[15] J. E. Shigley and J. J. Uicker, *Theory of Machines and Mechanisms*, McGraw-Hill, New York, NY, USA, 1980.

[16] S. P. Mermelstein and M. Acar, "Optimising cam motion using piecewise polynomials," *Engineering with Computers*, vol. 19, no. 4, pp. 241–254, 2004.

[17] H. Qiu, C.-J. Lin, Z.-Y. Li, H. Ozaki, J. Wang, and Y. Yue, "A universal optimal approach to cam curve design and its applications," *Mechanism and Machine Theory*, vol. 40, no. 6, pp. 669–692, 2005.

[18] R. G. Mosier, "Modern cam design," *International Journal of Vehicle Design*, vol. 23, no. 1/2, pp. 38–55, 2000.

[19] R. L. Norton, *Machine Design: An Integrated Approach*, pp. 111–116, Prentice-Hall, Upper Saddle River, NJ, USA, 2000.

[20] R. L. Norton, *Cam Design and Manufacturing Handbook*, Industrial Press, New York, NY, USA, 2009.

[21] A. Gabil and H. Baris, "Synthesis work about driving mechanism of a novel rotary dobby mechanism," *Tekstil Ve Konfeksiyon*, vol. 3, pp. 218–224, 2010.

[22] F. W. Flocker, "A versatile cam profile for controlling interface force in multiple-dwell cam-follower systems," *Journal of Mechanical Design*, vol. 134, no. 9, pp. 1–6, 2012.

[23] E. E. Peisekah, "Improving the polydyne cam design method," *Russian Engineering Journal*, vol. 12, pp. 25–27, 1966.

[24] M. P. Koster, "Vibrations of cam mechanisms," *Phillips Technical Library Series*, Macmillan Press, London, UK, 1974.